Advanced Powder Technology 33 (2022) 103429

Contents lists available at ScienceDirect

Advanced Powder Technology

journal homepage: www.elsevier.com/locate/apt

Formation and textural characterization of size-controlled $LaFeO_3$ perovskite nanoparticles for efficient photocatalytic degradation of organic pollutants

Kamal M. S. Khalil *, Abdelrahman H. Mahmoud, Mohamed Khairy *

Chemistry Department, Faculty of Science, Sohag University, Sohag 82524, Egypt

ARTICLE INFO

Article history:
Received 18 October 2021
Received in revised form 28 December 2021
Accepted 9 January 2022

Keywords:
$LaFeO_3$
Perovskites
Photo-Fenton-like catalyst
Sol-gel
Reusable catalyst

ABSTRACT

A series of $LaFeO_3$ perovskite nanoparticles (NPs) were successfully formed by a direct sol-gel method involving different citric acid to metal ratios of x (where x = 2–16). The resulted precursors were treated *via* auto-combustion, followed by calcination at different temperatures (300–700 °C). Size-controlled $LaFeO_3$ NPs were getting smaller down to 18.8 nm at high citric acid ratio, showing relatively high surface area up to 27.6 m^2/g . Photocatalytic activity of the formed $LaFeO_3$ NPs was explored for methylene blue (MB) degradation in the absence and presence of 0.5 mM H_2O_2 under light irradiation. Results showed that variation of citric acid to metal ratio alter the band gap and reduce the photo-generated charge carriers recombination of $LaFeO_3$ NPs. Moreover, the LFC4-500 material ($LaFeO_3$ synthesized using × = 4, and calcined at 500 °C) was the most active photocatalyst in solution at pH = 3 and 0.5 mM H_2O_2, with the highest efficiency > 99% within 30 min and showed excellent reusability without etching even after several cycles. Significantly, the $LaFeO_3$ NPs characteristics were correlated with their synthesis conditions and the type of interaction with citric acid during initial stages of crystal formation.

© 2022 Society of Powder Technology Japan Published by Elsevier B.V. All rights reserved.

1. Introduction

Discharge of organic contaminants from agricultural, textile, petrochemical, dying, painting, cosmetic, and pharmaceutical industries in water supplies cause serious problems for human, animal, and the aquatic environment [1]. Biological degradation, physical separation, and chemical treatment technologies were utilized for the removal of organic contaminants from wastewater [2–4].The biodegradable contaminants can be treated using microorganisms through a slow biological treatment process [5]. However, the complete removal of persistent organic contaminants from the environment is imperative and represents a great challenge. The chemical oxidation has been encouraged as a promising, efficient, economical, and acceptable methodology for large-scale wastewater treatment [6]. Advanced oxidation processes (AOPs) particularly Fenton reaction (Fe^{2+}/H_2O_2) and Fenton-like reactions (Fe^{3+}/H_2O_2) received much attention because they can produce nonselective and highly reactive hydroxyl radicals, which offer an eco-friendly technology for efficient degradation of persistent organic contaminants. Typically, a homogenous Fenton reaction includes a combination of dissolved ferrous ions and hydrogen peroxide (H_2O_2). However, the application of homogenous Fenton reaction in large-scale industry is limited because (*i*) the activity of ferrous ions is pH-dependent and (*ii*) difficult separation of the catalyst from the ultimate effluent. Therefore, the heterogeneous Fenton or Fenton-like catalytic reactions were developed by utilizing iron-based materials. Iron oxides [7,8], iron oxyhydroxide [9], metal ferrites [$M_xFe_{3-x}O_4$ (M = Zn, Mn, Co)][10], $BiFeO_3$[11], graphene-$BiFeO_3$[12], $SrFeO_{3-x}$[13] and iron oxide NPs immobilized on mesoporous silica were studied [14]. Furthermore, the catalytic efficiency was enhanced by utilizing external energy such as UV light, microwave, electricity, and ultrasound radiation [15]. Although the tremendous research efforts in the heterogeneous Fenton reactions, sluggish Fe(II) regeneration kinetics, low reaction efficiency, and high H_2O_2 consumption are still the major challenges. To overcome these limitations, the control synthesis of iron-based catalysts in terms of structural, compositional, and electronic properties and their catalytic activity progress under photonic, electric, and ultrasonic driven forces should be addressed.

Light-driven photo-Fenton reaction was explored recently as a highly promising approach to boost = Fe (II) regeneration and H_2O_2 activation compared to the other heterogeneous Fenton processes. Fortunately, most iron oxides and ferrite are

---

* Corresponding authors.

E-mail addresses: kms_khalil@yahoo.co.uk (K. M. S. Khalil), mohamed.khairy@science.sohag.edu.eg (M. Khairy).

https://doi.org/10.1016/j.apt.2022.103429

0921-8831/© 2022 Society of Powder Technology Japan Published by Elsevier B.V. All rights reserved.

semiconductors that have narrow band gaps, which might interact with visible light irradiation [16,17]. However, the short transfer distance of photo-generated charge carriers (hole/electron pairs) leading to a fast recombination rate and thus reducing the overall photocatalytic efficiency. Perovskites are well known as multi-hole semiconductors that show interesting applications in photocatalysis [18]. Perovskite-type oxides have a general formula ABO_3, where A, and B are rare earth metal ions and transition metal ions, respectively. Interestingly, the band gap energy of ABO_3 can be tuned by altering the A and B ions or doping of different ions in the perovskite crystal lattice. Among the ABO_3 perovskites, Lanthanum orthoferrite ($LaFeO_3$) is a promising visible-light-driven photocatalyst. It is a *p*-type semiconductor with narrow band gap energy between 2 and 2.6 eV and unique optoelectronic properties [19,20]. It has an orthorhombic structure, consists of FeO_6 octahedron units and La^{3+} lies in between these units. Thanks to their thermal and chemical stability, $LaFeO_3$ mixed metal oxide has been used in many potential applications such as sensors [21], water splitting [22], photocatalysis [19,23,24], and solid oxide fuel cells [25]. Since, the characteristics of $LaFeO_3$ are mainly depending on the stoichiometric ratio, surface morphology, and particle size, several synthetic strategies including; sol-gel [26], microwave-assisted thermal decomposition [27], hydrothermal [28], sonochemical [29], co-precipitation, and low-temperature thermal decomposition were recently reported [30]. The sol-gel method is one of the most successful methods for large-scale production of nanostructured $LaFeO_3$. However, the $LaFeO_3$ NPs tend to agglomerate at high temperatures. Hence, the active sites for photocatalytic degradation efficiency will be sequentially reduced. The $LaFeO_3$ NPs were successfully dispersed on different porous supports. Formation of high surface area and thermally stable $LaFeO_3$ nanocomposite were recently achieved by our group *via* the dispersion of their citrate precursors in nonporous silica [31] and ordered mesoporous MCM-41 silica [32].Other dispersion phases were reported such as TiO_2 nanotubes [19] and carbon [33]. To the best of our knowledge, crystal size control of $LaFeO_3$ to nanosized level from a single precursor has not been explored yet.

In this context, a series of size-controlled $LaFeO_3$ NPs were formed by using of a direct sol-gel auto-combustion method. The crystallinity, band gap and particle size were effectively controlled using different molar ratio of citric acid (x = 2, 4, 8, and 16), and subsequently calcination at different temperatures (300, 500, 600, and 700 °C). The obtained materials showed very interesting structural, textural, morphological properties, which reflected on their optical and photocatalytic activity towards MB decolorization as a model of organic contaminants, under-stimulated sunlight. MB is widely discharged from many agricultural and industrial activities in water supplies causing intensive harmful effects. Therefore, removal of MB from these effluents is a very important issue for many current researches. The optimized conditions for photocatalytic experiments were investigated and the decolorization mechanism of MB was also proposed by using electron, hole, and radical scavengers.

2. Experimental and method

2.1. Materials

All chemicals were of the highest analytical grade available used without further purification. Lanthanum nitrate hexahydrate ($La(NO_3)_3{\cdot}6H_2O$, 99%), citric acid $C_6H_8O_7$ (98%), and Ferric nitrate nanohydrate $Fe(NO_3)_3{\cdot}9H_2O$ were purchased from Alpha chemical Co. LTD. Hydrogen peroxide (H_2O_2, 30%), Ammonium hydroxide (NH_4OH, 33%), and methylene blue (MB) were purchased from BDH Chemicals Ltd. Hydrochloric acid (HCl, 37%) obtained from RIEDEL-DE HAEN company. Sodium persulphate, EDTA, *t*-butyl alcohol, and sodium hydroxide were purchased from Sigma Aldrich Co. Ltd.

2.2. Formation of $LaFeO_3$ NPs.

The $LaFeO_3$ materials were synthesized by a direct sol-gel auto-combustion method using citric acid as a complexing agent with molar ratios (x = 2, 4, 8, and 16). The stoichiometric amount of ferric nitrate nanohydrate $Fe(NO_3)_3{\cdot}9H_2O$ (5 mmol) and lanthanum nitrate hexahydrate $La(NO_3)_3{\cdot}6H_2O$ (5 mmol) were dissolved in 100 mL doubly distilled water under continuous stirring. Then, a solution of citric acid was dropwise added. The pH of the aforementioned mixture was adjusted by the addition of NH_4OH to reach pH 8 and stabilize the nitrate-citrate sol. Homogenous nitrate-citrate sols were produced and stabilized at room temperature for one hour under magnetic stirring. The resultant sols were dried overnight at 120 °C. Dried gel materials were chars gradually after their drying in the order of LFC16 > LFC8 > LFC4 > LFC2 precursors due to the expected oxidation of citric acid species at low temperature. It is known that, the charring process of citric acid led to dehydration, CO_2 loss and fragmentations into small species at low temperature, specially, in presence of some nitrate species. The dried gels were transferred into a dried crucible and ignited by a Benzen stove to form a fluffy powder. Then, the final products were calcined at different temperatures (300, 500, 600, and 700 °C) for 1 h at a heating rate of 1 °C/min. The produced $LaFeO_3$ samples were assigned as LFCx-yyy, where (x) represents citric acid molar ratio, and (yyy) is corresponding to calcination temperatures. The $LaFeO_3$ materials were then used for further photocatalytic reactions.

2.3. Characterization of $LaFeO_3$ NPs.

The X-ray diffraction pattern of $LaFeO_3$ materials was recorded using D8-advance X-ray diffraction with monochromatic Cu-K_α radiation (λ = 1.5418 Å), and a scan rate of 0.05°/min in the 2θ range from 10° to 80°. The diffraction patterns were analyzed using PDF-2 Release 2009. Fourier transform-infrared (FTIR) spectroscopy in the attenuated total reflectance (ATR) mode of $LaFeO_3$ samples was carried out using the Bruker Alpha FTIR instrument in the range 400–4000 cm^{-1} using KBr to investigate the chemical functional groups. Simultaneous Thermogravimetric-Differential (TG-DTA) thermal analyses were obtained using a thermal analyzer model sdt q600 v20.9 build 20. TGA and DTA thermograms were collected during heating up, with a ramp rate of 10 ○C/min, from room temperature (RT) to 900 °C in a flow of air atmosphere at 50 mL/min.

The diffuse reflectance spectra of $LaFeO_3$ samples and the absorbance measurements of MB were performed at UV/VIS/NIR spectrophotometer model JASCO 770 V. Textural properties and specific surface area of $LaFeO_3$ samples were determined by measuring N_2 adsorption/desorption isotherms at 77 K using BELsorp-mini, Japan. Before N_2 adsorption/desorption measurements, the $LaFeO_3$ samples were degassed using flow N_2 gas (99.999%) at 300 °C for 8 h. The specific surface area (S_{BET}) was calculated by the Brunauer-Emmett-Teller (BET) and and pore size distribution was derived by Barrett-Joyner-Halenda (BJH) methods.

Transmission electron microscopy model JEOL JEM model 2100F was used to explore the morphology of $LaFeO_3$ samples. The $LaFeO_3$ samples were grinded, dispersed in ethanol and dropped on a copper grid. Prior to inserting the $LaFeO_3$ into the TEM column, the grid was vacuum dried for 20 min.

2.4. Set-up of the photocatalytic experiment.

The photocatalytic experiments were carried out using a cylindrical reactor made from quartz with a total capacity of

50 mL surrounded by a circulating water jacket to keep solution temperature at 30 °C. The reactor was placed horizontally in front of a 75 W xenon lamp producing a wide range of wavelengths to simulate sunlight. The reactor was positioned away from the lamp with light intensity simulated 1 sun (100 mW cm^{-2}) using a Thorlabs digital handheld energy meter console (PM100D) connected with a calibrated high sensitivity thermal sensor (S401C, Thorlabs).

The photocatalytic experiment was carried out at different pHs, $LaFeO_3$ NPs dosage, and H_2O_2 concentrations in presence of 10 mg/L MB at ambient temperature. Based on our results, the mixture was purged with nitrogen and stirred in dark for 30 min to reach adsorption/desorption equilibrium before irradiation [10,23]. The photocatalytic experiments were carried out in three replicates. The decrease in MB concentrations was monitored by measuring the absorbance at λ_{max} = 655 nm. The decolorization of MB in absence of catalyst was also investigated using a xenon arc lamp and monochromatic light source at λ_{max} = 365 nm. It was found that; the decolorization efficiency of MB is negligible compared to $LaFeO_3$ photocatalyst. The pH 3 was selected to be an optimum medium for MB decolorization over $LaFeO_3$ under-stimulated solar light irradiation. A 50 mL cylindrical reactor involves 10 mg/L of MB and 10 mg of $LaFeO_3$ sample was magnetically stirred in dark for 30 min to reach adsorption/desorption equilibrium. Then, H_2O_2 was added to the mixture to initiate the photo-Fenton-like reaction. At interval time, 4 mL of the reaction mixture was withdrawn, centrifuged to separate the aqueous phase from the solid catalyst, and the transparent solution was then analyzed by UV/VIS/NIR spectrophotometer. The absorbance is corresponding to C_0. After that, the reactor was illuminated with a xenon lamp under continuous stirring for 120 min and 60 min in the absence and presence of H_2O_2, respectively [24]. At a regular interval, 4 mL of the mixture was taken out, centrifuged, and measured the absorption intensity corresponding to C_t. The photocatalytic efficiency was calculated using the following relationship;

$$Efficiency(\%) = \frac{(C_o - C_t)}{C_0}\% \tag{1}$$

3. Results and discussion

3.1. Characterization of the catalyst

The $LaFeO_3$ NPs were synthesized using a sol-gel auto-combustion method in presence of different molar ratios of complexing agents i.e. citric acid (*x* = 2, 4, 8, and 16). Fig. 1(a-d) shows wide-angle X-ray diffraction patterns of $LaFeO_3$ materials calcined at different temperatures (300, 500, 600, and 700 °C). Typical diffraction peaks of $LaFeO_3$ material were presented in the range of 2θ from 10° to 80°, clarifies that all $LaFeO_3$ materials have a well crystalline phase. The characteristic diffraction peaks of $LaFeO_3$ phase located at $2\theta^o$ = 22.38°, 32.03°, 39.54°, 46.03°, 57.26°, 67.20°, and 76.47°, that corresponding to (101), (121), (220), (202), (312), (242), and (420), respectively. These peaks were assigned to orthorhombic structure (JCPDS 37-1493) with a space group *Pnma* and lattice parameters a = 5.566 Å, b = 7.854 Å, and c = 5.553 Å. Further, there are no additional secondary diffraction peaks regarding La_2O_3 or Fe_2O_3 confirming a pure phase of $LaFeO_3$ nanocrystals [23]. The intensity of the diffraction peaks was enhanced by increasing the calcination temperatures. Further, the intensity of the diffraction peaks at a ratio of 4 is the highest amongst other citric acid molar ratios. It was found, the increase of the citric acid ratio retards the formation of large crystals of $LaFeO_3$ even at higher temperatures. Therefore, the citric acid ratio is a crucial prerequisite for the formation of highly crystalline $LaFeO_3$ materials of multiple sizes. High crystalline $LaFeO_3$ materials can be obtained at a citric acid molar ratio of 4 even at a moderate temperature > 300 °C. The crystal size was calculated using the *Debye-Scherrer* equation as follow;

$$D_p = \frac{0.94\lambda}{\beta_{\frac{1}{2}}(cos\theta)} \tag{2}$$

where λ is a radiation wavelength (1.518 nm), $\beta_{1/2}$ is the full width of half maximum of peak intensity in radian and θ is a Bragg angle in degree. The D_p represents a grain or crystal size in nm. The crystal size of $LaFeO_3$ samples were calculated and found in the range of 18.83–29.34 nm as shown in Fig. S1 and Table 1. The crystal size was increased at elevated calcination temperature, which is in agreement with XRD data reported by *Köferstein et al.* [34]. The crystallite size of $LaFeO_3$ NPs was enhanced at all calcination temperatures by increasing the citric acid ratio from 2 to 4, followed by a noticeable decline for ratios 8 and 16. *Thirumalairajan et al.* suggested that the citric acid ratio of 2 was necessary to obtain a pure $LaFeO_3$ crystal without the presence of any secondary products such as La_2O_3, Fe_2O_3, and $La(OH)_3$ [23]. However, the suggested sol-gel procedure offered a pure $LaFeO_3$ crystal with a controlled grain size by adjusting only the molar ratio of complexing agent i.e. citric acid even at different calcination temperatures.

To investigate the surface functional groups, FTIR spectroscopy of $LaFeO_3$ NPs was carried out in the range of 400–4000 cm^{-1} at different citric acid ratios and calcination temperatures as shown in Fig. 2 (a - d). The FTIR spectra were analyzed by matching with the previously reported FTIR spectra of $LaFeO_3$ materials [35–37,40–44]. The absorption bands at 453, and 575 cm^{-1} are attributed to O–Fe–O deformation vibration and Fe–O stretching vibration, respectively, being characteristic of the octahedral FeO_6 group in $LaFeO_3$ [23,35]. The characteristic peaks related to Fe–O, which enhance and become sharper at the high calcination temperature. These observations are in agreement with the XRD data since the intensity of diffraction peaks were increased at elevated temperatures. A small band located at 847 cm^{-1} is assigned to asymmetric stretching modes of the carbonate ions. The bands located at 1402 and 1494 cm^{-1} are characteristic absorption peaks of asymmetric stretching of metal carbonates, which cannot be detected using XRD [36]. The absorption band at 1647 cm^{-1} is related to C = O of carboxylic group and 2355 cm^{-1} are related to asymmetric and symmetric stretching vibrations of carboxyl root [23,37]. Noticeably, these absorption bands were increased at a high citric acid ratio. The observed broad band at 3421 cm^{-1} is attributed to H–O stretching vibration modes or physically absorbed water on the particle surface [23]. The intensity of the hydroxyl group band was reduced with increasing the calcination temperatures. The absorption band located at 3608 cm^{-1} which appeared only at a high calcination temperature of 700 °C is characteristic of La-O [35]. These results confirm the formation of a pure $LaFeO_3$ crystal combined with carbon residues.

Simultaneous TGA-DTA analysis was carried out for the $LaFeO_3$ materials pre calcined at 300 °C in the flow of air atmosphere. The TGA curves along with their DTG curves are shown in Fig. 3 (A), and DTA curves are shown in Fig. 3 (B), respectively. The measured weight losses at fixed temperatures of 300, 500 and 700 °C were calculated to estimate the percentage of carbon in the $LaFeO_3$ samples. The weight loss in the range of 200–350 °C was found to be 1.3, 2.0, 2.3, and 2.7%, while the weight loss found to be 8.8, 14.7, 6.66, and 10.7% upon heating to 500 °C for LFC2, LFC4, LFC8 and LFC16, respectively. Meanwhile, the total weight losses upon heating to 700 °C are 11.0, 17.7, 8.9, and 12.9% for LFC2, LFC4, LFC8 and LFC16, respectively. It seems that the LFC4 sample was containing the highest percentage of carbonaceous material compared to LFC8 and LFC16 (prepared with the high ratio of citric acid). Such behavior might be related to the formation of different of $M \leftarrow L_n$ com-

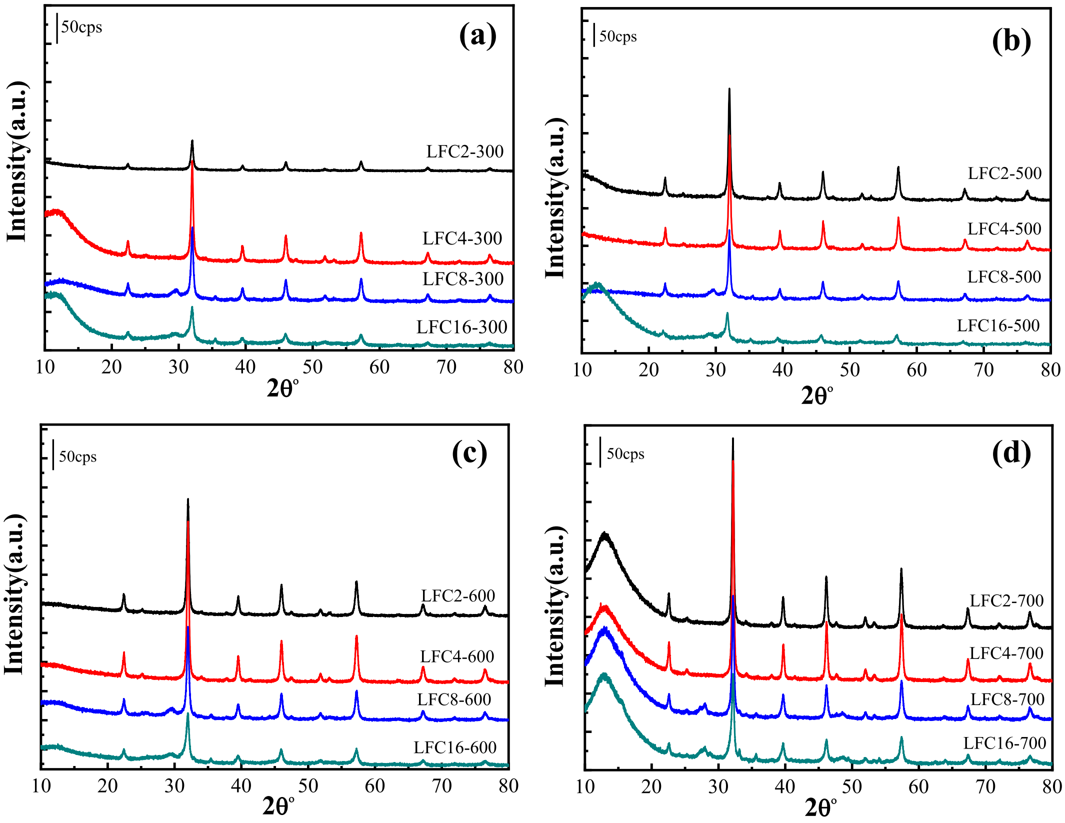

Fig. 1. XRD patterns of $LaFeO_3$ samples synthesized using different molar ratio of citric acid and calcined at (a) 300 °C (b) 500 °C (c) 600 °C (d) 700 °C.

Table 1
The calculated crystal size of $LaFeO_3$ derived from XRD patterns.

Sample	Crystal size(nm)	Sample	Crystal size(nm)	Sample	Crystal size(nm)	Sample	Crystal size(nm)
LFC2-300	24.9	**LFC2-500**	26.5	**LFC2-600**	25.4	**LFC2-700**	29.1
LFC4-300	26.6	**LFC4-500**	29.1	**LFC4-600**	26.4	**LFC4-700**	29.3
LFC8-300	25.2	**LFC8-500**	26.3	**LFC8-600**	25.2	**LFC8-700**	26.7
LFC16-300	18.8	**LFC16-500**	19.5	**LFC16-600**	19.9	**LFC16-700**	23.0

plexes (L = citrate ligands, M = Fe^{3+} or La^{3+} ions). Noting that the $LaFeO_3$ materials were calcined in air at 300 °C before the TGA measurements. This treatment may led to the decomposition of non-bonded citrate species for LFC8 and LFC16 at $\leq$ 300 °C, and these species are supposed to be weakly coordinated or non-coordinated species. This was justified in terms of the previously reported studies that different LM species are formed at different M:L ratios [38]. It has been found [39] that ferric citrate speciation is significantly dependent on the excess of citrate species available in the solution. Thus, at low citrate: Fe(III) molar ratios, the oligomeric species such as trinuclear complexes of $[Fe_3O(Cit)_3H_3]^{2-}$ are the most abundant species; and the mononuclear species of $[Fe(Cit)_2H_4]^{-}$ was dominating at high citrate: Fe(III) ratios [39]. This indicates that the excess citrate will be present as free (non-bonded) species at high high citrate: Fe(III) ratios. Thus, the decomposition of such excess free (non-bonded) species was supposed to occur during the ignition step at 300 °C before the TGA measurements. However, the small DTG peak observed at 320 °C, with intensity in the order of LFC4 < LFC8 < LFC16, can be assigned to the presence of residual part of free (non-bonded) citrate species.

Therefore, the main DTG peak for the different samples, which was peaking at 410 °C, assigned to the decomposition of strongly bonded (to the M^{n+} ions) species. Intensity of the latter peak was following the order of LFC4 > LFC16 < LFC2 < LFC8. Furthermore, a small DTG peak was observed at 620 °C (for LFC2 and LFC4) and at 660 °C (for LFC8 and LFC16), which may be assigned for the combustion of residual carbon/carbonate species. The residual carbon contents were found to be 2.3, 3.0, 2.4, and 2.2% for LFC2, LFC4, LFC8, and LFC16, respectively.

The DTA Curves (Fig. 3b) confirms the above assignment about the presence of strongly bonded citrate species for in the LF4 sample. The observed peak maxima and peak areas are in the same order of the weight loss LFC2 < LFC4 > LFC16 > LFC8. Thus, it can be concluded that the oligomer species of $[M_3O(Cit)_3H_3]^{2-}$ were the most abundant species in LFC2 and LFC4 precursors, whereas mononuclear complex $[M(Cit)_2H_4]^{-}$ were predominate in LFC8 and LFC16. This implies that citrate species are more bonded at low ration, whereas more non bonded, easy to burn, species are present at high ratios.

The optical band gap energy of perovskite oxide material is one of the significant key factors for determining the photocatalytic activity. To recognize the effect of citric acid and calcination temperatures on the optical band gap, the optical properties of $LaFeO_3$ were investigated using UV/Vis spectroscopy. Fig. 4 shows diffuse reflectance spectra of $LaFeO_3$ materials synthesized using various citric acid ratios and treated at different calcination temperatures which is equivalent to the absorbance. The R% values were

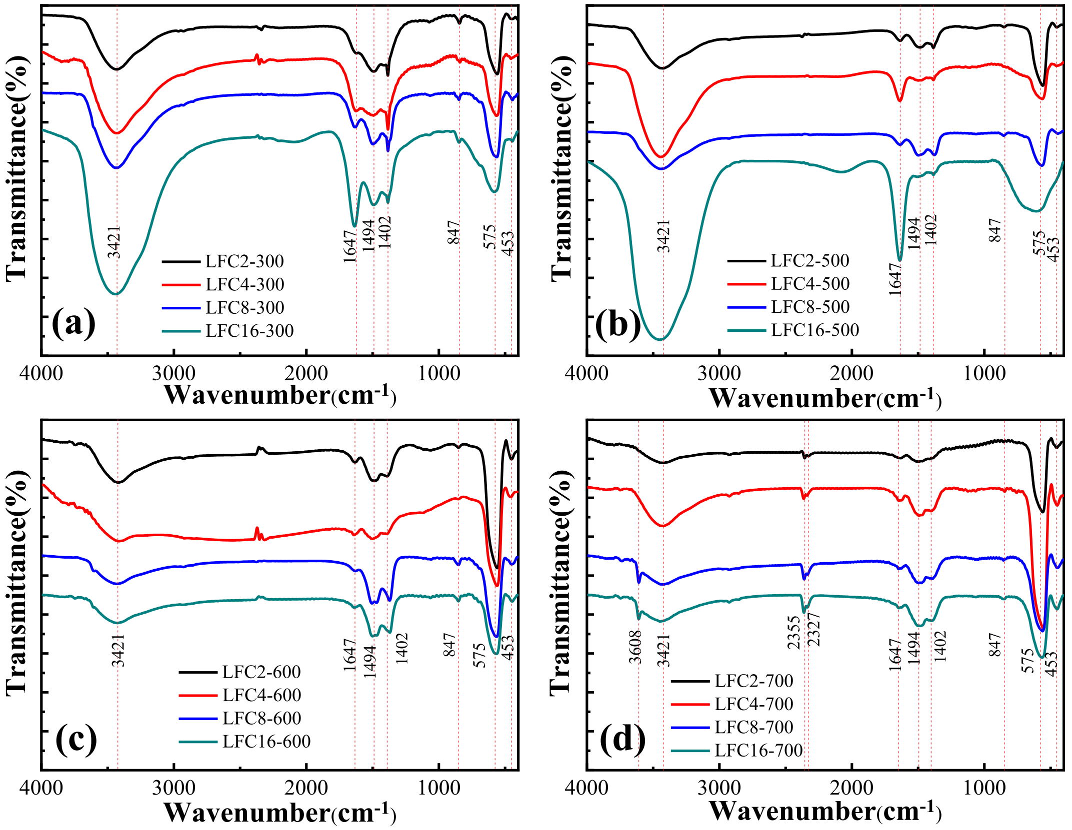

Fig. 2. FTIR spectra of $LaFeO_3$ samples synthesized using different molar ratio of citric acid and calcined at (a) 300 °C (b) 500 °C (c) 600 °C (d) 700 °C.

increased to almost 100% at $\lambda > 600$ nm, indicating that, the $LaFeO_3$ materials absorb light in the visible region. The strong absorption is mainly related to the electronic transition from the valance band to the conduction band, $O_{2p} \rightarrow Fe_{3d}$. Thus, $LaFeO_3$ could serve as a potential visible-light-driven-photocatalyst. The optical band gap of $LaFeO_3$ was accurately determined utilizing diffuse reflectance measurements through *McLean* analysis of the absorption edge as shown in the following equations [34,40].

$$\alpha h\nu = k(h\nu - E_g)^{1/n} \tag{3}$$

$$F(R).h\nu = k(h\nu - E_g)^{1/n} \tag{4}$$

Where α is the absorption coefficient, h is Planck's constant, ν is irradiation frequency, E_g is optical band gap energy, and k is the energy-independent constant. The type of electronic transition can be determined based on a value of n which usually takes 2, 2/3, 1/2, and 1/3 values for direct allowed transition, direct forbidden transition, indirect allowed transition, and indirect forbidden transitions, respectively. The best fit of the straight line near to the absorption edge was achieved at n = 2 by plotting the relation between $(F(R).h\nu)^n$ *vs.* hν (as shown inset Fig. 4) [34]. The direct allowed transition was exploited, and the Eq. (4) can be transformed to,

$$F(R).h\nu = k(h\nu - E_g)^{1/2} \tag{5}$$

The band gap energy (E_g) of $LaFeO_3$ materials was determined and presented in Table 2 by extrapolation of the linear part at the energy of F(R) → 0. The values of E_g were varied from 2.381 eV for LFC8-500 to about 2.557 eV for the LFC2-700 sample. The band gap values do not change significantly upon thermal treatment at elevated temperatures which in agreement with previous studies [34,41]. Further, the values of the band gap were notably reduced with increasing citric acid ratio up to 8 and then increased at a ratio of 16 (Fig. S2). The band gap energy of LFC2-500 and LFC4-500 materials with a crystal size of 26.47 and 29.06 were estimated to be 2.53 and 2.47 eV, respectively. This behavior might also confirm the presence of a functionalized carbon around $LaFeO_3$ NPs, particularly at a higher citric acid ratio 16. *Wang and coworkers* synthesized $LaFeO_3$ immobilized onto the carbon sphere *via* an ultrasonic-assisted method [34]. The band gap values were decreased from 2.12 eV to 1.43 eV for $LaFeO_3$ and $LaFeO_3$/C, respectively. The presence of carbon enhances the corresponding photocurrent due to the lowering of the recombination rate of electron-hole pairs in visible light absorption. Thus, a study of citric acid ratio upon crystallization of $LaFeO_3$ materials is a critical issue to control the band gap and their photocatalytic applicability.

The position of valance band (VB) and conduction band (CB) edges of $LaFeO_3$ materials at a point of zero charge were estimated using Eq. (6) [45].

$$E_{CB} = \chi - E_e - 0.5E_g \tag{6}$$

where E_{CB} and E_{VB} are the potentials of conduction and valance band edges, respectively, χ is the absolute *Mulliken* electronegativity of the constituent elements for the semiconductor, E_e is the energy of free electron on hydrogen scale (~4.5 eV). The χ value of $LaFeO_3$ is ca. 5.54 eV. The potentials of conduction and valance band edges of $LaFeO_3$ samples were estimated as shown in Table S3. The calculated values of E_{CB} are −0.22, −0.19, −0.15, and −0.17 eV *vs.* NHE for LFC2-500, LFC4-500, LFC8-500, and LFC16-500, respectively. Meanwhile, the potential of valance band edge was calculated by the following equation;

$$E_{VB} = E_{CB} + E_g \tag{7}$$

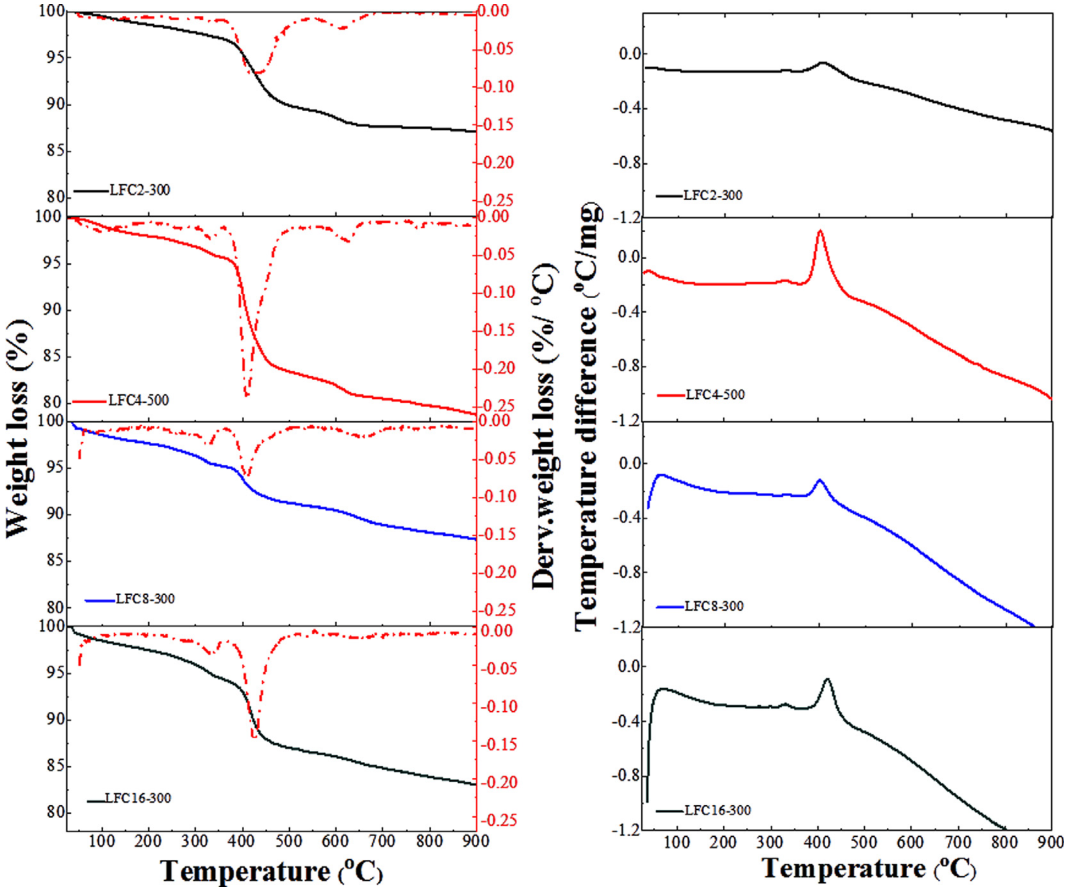

Fig. 3. (a) TGA-DTG and (b) DTA analysis of $LaFeO_3$ samples synthesized using different ratio of citric acid.

The calculated values of E_{VB} are 2.31, 2.28, 2.23, and 2.26 eV *vs.* NHE for LFC2-500, LFC4-500, LFC8-500, and LFC16-500, respectively.

Next attention was turned to investigate the morphological characteristics of $LaFeO_3$ in presence of various citric acid ratios. Fig. 5 shows the TEM micrographs of $LaFeO_3$ materials synthesized using different molar ratios of citric acid calcined at 500 °C. Aggregated spherical $LaFeO_3$ NPs were observed. The average sizes are 25, 35, 15, and 17 nm for the citric molar ratio of 2, 4, 8, and 16 respectively. The particle size increases from ratio 2 to 4 and then decreases in ratios 8 and 16 which in agreement with the XRD data. The carbon residues (which were detected by TGA) were very significant at a M: citric ratios to produce highly porous structures as observed in Table 3. Further, the particle size was increased at elevated calcination temperatures as shown in Fig. S4. Thus, manipulation of citric acid ratios might have a significant effect not only on the crystal size but also on the structure of grain boundaries.

The heterogeneous catalytic process commonly occurs at solid catalyst surface. Accordingly, the solid catalyst with large high surface area is more favorable because the porous network increased the area of exposed active sites to reactants molecules. The textural properties of $LaFeO_3$ materials were measured using N_2 adsorption/desorption isotherms as shown in Fig. 6. According to IUPAC classifications, the $LaFeO_3$ materials exhibited type IV isotherm with an H_3 hysteresis loop at a high relative pressure region, which is characteristic of mesoporous nature. The *meso*-cavities produced through the interconnected $LaFeO_3$ NPs or extended carbon at a high citric acid ratio as shown in TEM images. The specific surface area (S_{BET}) of $LaFeO_3$ materials was derived from the *Burner-Emmett-Teller* method and represented in Table 3. The S_{BET} values were found in the range 12–27.6 m^2/g which are higher than the previously reported values [23,32,34]. It was found the materials calcined at 500 °C have a higher surface area for different citric acid ratios and then decreased at elevated temperatures. Therefore, the materials calcined at 500 °C might show high photocatalytic activity. Further, the S_{BET} was increased with increasing the molar ratio of citric acid except ratio 4, due to removing of carboneous materials, which formed through burning of oligomer species. The pore size distribution was derived from the adsorption curve by the *Barrett-Joyner-Halenda* (BJH) method (Fig. 6b). Multi-directional pore size distribution in the range of mesoporous region was observed for all synthesized $LaFeO_3$ NPs. Such a porous network offers accessible pores which significantly enhances the diffusion of ions to the active sites and increases photocatalytic efficiency.

3.2. The photocatalytic activity of $LaFeO_3$.

The photocatalytic activity of perovskite materials is primarily influenced by metal cation and/or oxygen anion vacancies in the orthorhombic unity cell, which offered a significant increase in adsorbed oxygen molecules at the surface. As a result, the effective electron/hole separation might be achieved by the additional holes trapping in the distorted crystal lattice. The manipulation of crystal size and band gap energy of $LaFeO_3$ by tuning of citric acid ratio was presented in this context and will be explored for photocatalytic decolorization of MB as a model of organic pollutants. Fig. S5a shows the effect of solution pH on MB decolorization by introducing a 0.10 g/L LFC4-500 dosage in a reactor containing 10 mg/L MB in different pHs of 3, 5, 7 and 9 for one-hour

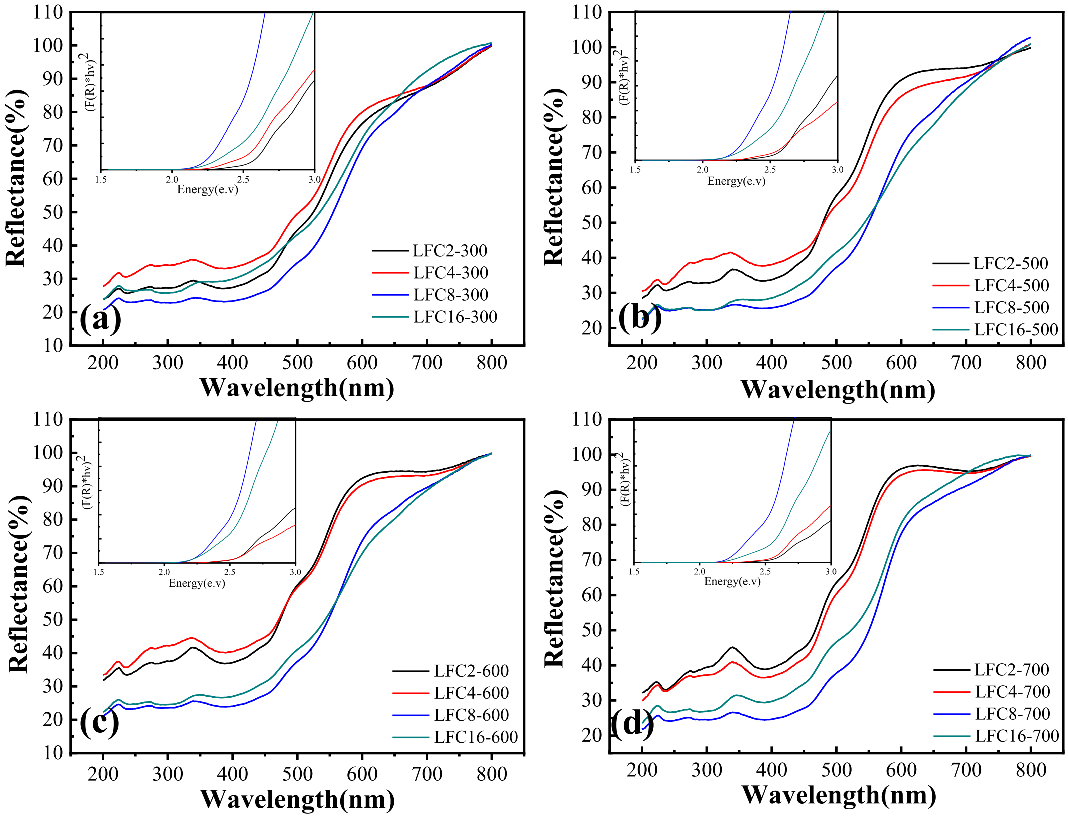

Fig. 4. Diffuse reflectance spectra of $LaFeO_3$ samples synthesized using different molar ratio of citric acid and calcined at (a) 300 °C (b) 500 °C (c) 600 °C (d) 700 °C. (Inset Tauc plot of the relation between F(R)*hν *vs.* E (eV).

Table 2
The calculated bandgap energies of $LaFeO_3$ at different conditions.

Sample	E_g (eV)	Sample	E_g (eV)	Sample	E_g (eV)	Sample	E_g (eV)
LFC2-300	2.54	**LFC2-500**	2.53	**LFC2-600**	2.54	**LFC2-700**	2.56
LFC4-300	2.49	**LFC4-500**	2.47	**LFC4-600**	2.50	**LFC4-700**	2.54
LFC8-300	2.39	**LFC8-500**	2.38	**LFC8-600**	2.41	**LFC8-700**	2.49
LFC16-300	2.45	**LFC16-500**	2.43	**LFC16-600**	2.45	**LFC16-700**	2.50

under-stimulated solar-light irradiation. The solution pH has a synergic effect in photocatalytic decolorization of MB because it probably controls the surface charges or counterions around the $LaFeO_3$ NPs. The highest decolorization efficiency was observed in a solution of pH 3. These results are in agreement with previously reported literature [4,42].

For the photo-Fenton catalytic experiment, H_2O_2 concentrations, and $LaFeO_3$ dosage were investigated. Fig. S5b represents the efficiency of 0.10 g/L LFC4-500 sample for decolorization of 10 mg/L MB in absence and presence of 0.1 mM H_2O_2 at pH 3 in dark and under-stimulated solar light irradiation. The color of solution was changed to colorless with time. The photocatalytic efficiency was estimated to be 0.5%, 1.48%, 6.08%, 11.06%, and 45.45% within 30 min for H_2O_2 in dark, H_2O_2/solar-light (photolysis), LFC4-500/solar-light (photocatalysis), LFC4-500/H_2O_2 in dark (Fenton-like process) and LFC4-500 /H_2O_2/solar-light (photo-Fenton-like process), respectively. It was also observed that no catalytic efficiency of $LaFeO_3$ materials was observed in dark conditions. Interestingly, the combination of the $LaFeO_3$ and H_2O_2 under solar-light irradiation accomplished outstanding photocatalytic efficiency within a short reaction time due to in situ photo-generated highly reactive hydroxyl radicals ($HO^{\cdot}$) [4,8,9,14]. It was reported the photocatalytic efficiency was decreased in a higher pH value due to the undesirable H_2O_2 decomposition, relatively inactive ferryl ions formation, or generation of high-valent iron species. Therefore, a solution pH 3 was selected as the most appropriate conditions for further experiments. Further, the effect of H_2O_2 concentrations upon the decolorization of MB was also investigated (Fig. S5c). A 0.1 g/L of LFC4-500 sample was dispersed in a solution of pH 3 containing 10 mg/L MB and different H_2O_2 concentrations (0.2, 0.3 and 0.5 mM) under-stimulated solar light irradiation. The photocatalytic efficiency enhances with increasing H_2O_2 concentrations and reaches 72.3 %, 87.2 %, and 99.3% within 30 min of reaction time. These results demonstrated that the $LaFeO_3$ is an efficient photocatalyst for the MB decolorization even in the presence of low H_2O_2 concentrations. These results are very interesting compared to previously reported data shown in Table 4. Little hydroxyl radicals were produced at low H_2O_2 concentrations. However, at high H_2O_2 concentrations, the produced hydroxyl radical interacts with H_2O_2 and generates hydroperoxyl species, which likely scavenge active hydroxyl radicals [43]. Thus, a concentration of 0.5 mM H_2O_2 was utilized in the photo-Fenton reaction. The effect of LFC4-500 dosages was also explored in MB decolorization. It was found a dosage of 0.2 g/L is a sufficient dosage under our optimized conditions.

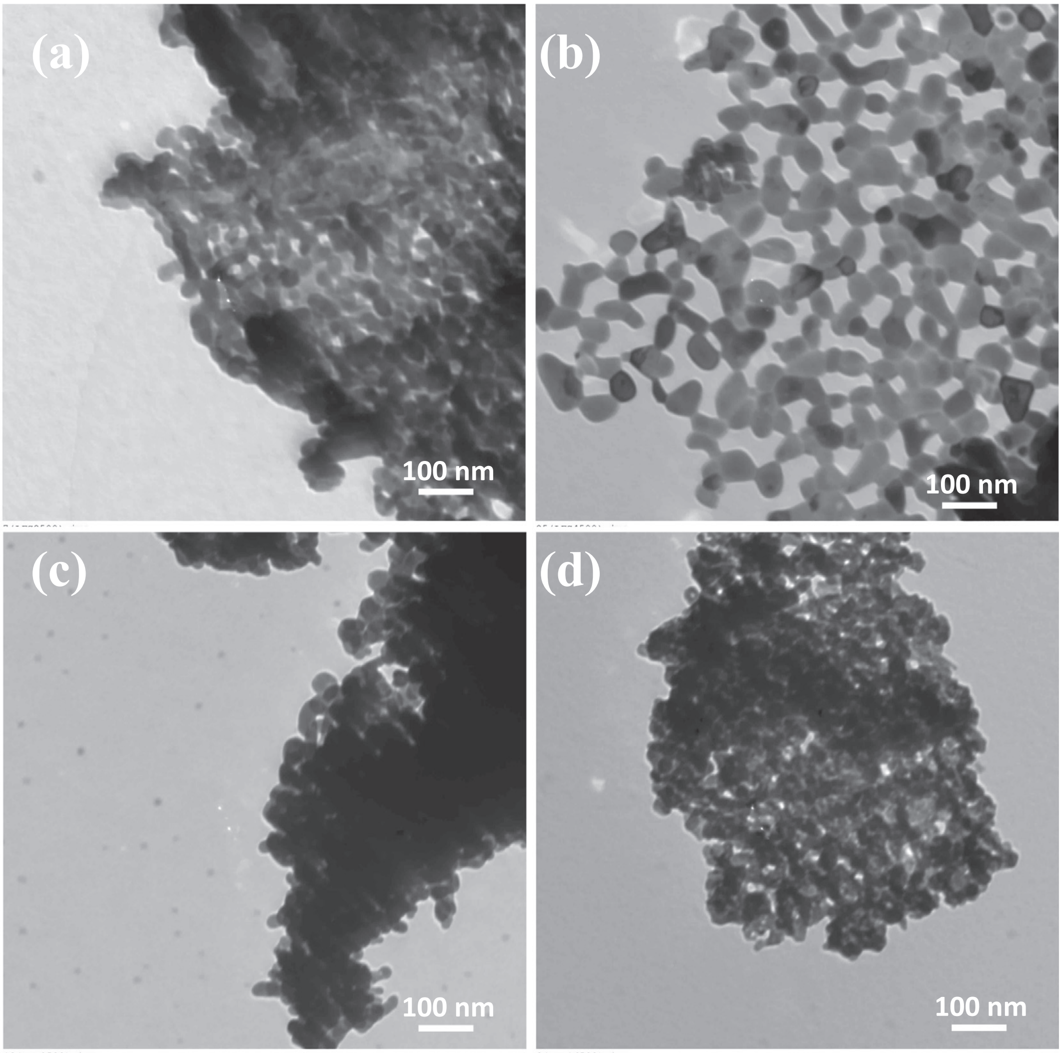

Fig. 5. TEM images of $LaFeO_3$ samples synthesized using different molar ratio of citric acid.

Table 3
Textural properties of $LaFeO_3$ materials at different conditions.

Citric ratio	**300 °C**			**500 °C**			**600 °C**			**700 °C**		
	S_{BET}(m^2g^{-1})	**D_p(nm)**	**V_p(cm^3g^{-1})**	**S_{BET}(m^2g^{-1})**	**D_p(nm)**	**V_p(cm^3g^{-1})**	**S_{BET}(m^2g^{-1})**	**D_p(nm)**	**V_p(cm^3g^{-1})**	**S_{BET}(m^2g^{-1})**	**D_p(nm)**	**V_p(cm^3g^{-1})**
2	15.5	1.96	0.024	21.0	10.9	0.092	17.2	12.52	0.083	14.1	2.21,	0.082
4	12.1	2.21	0.031	16.9	10.9	0.084	16.1	10.9	0.095	12.7	2.21	0.071
8	21.9	1.74	3.688	23.8	10.9	0.1433	23.9	10.9	0.1283	18.8	10.9	0.12
16	22.3	2.21	5.161	27.6	10.9	0.1461	24.1	10.9	0.1181	18.8	1.96	0.091

The UV/Vis spectra of MB decolorization using $LaFeO_3$ materials were represented in the absence and presence of H_2O_2 under solar irradiation as shown in Figs. 7, S6 and S7. The spectra of MB were altered obviously during photocatalytic process in the presence of H_2O_2. All the absorption bands at $\lambda = 245, 290, 614$, and 655 nm are gradually decreased. These peaks might be assigned to the benzene ring, phenothiazine conjugate system, and auxochrome group, respectively. The reduction of these peaks might be related to destruction of sulfur-nitrogen conjugated system and ring-opening reaction of phenothiazine [58,59]. Further, the absorbance of the MB solution with $LaFeO_3/H_2O_2$ approach almost zero after 60 min, indicating a complete decolorization/degradation of MB. It was found the photocatalytic efficiency of $LaFeO_3$ materials is effectively controlled by the variation of citric acid ratios. The photocatalytic efficiency of $LaFeO_3$ fabricated by citric ratios 8 and 16 is negligible at all calcination temperatures. This might be due to the small particle size, narrow bandgap and low carbon residual content of LFC8 and LFC16 samples which promotes the recombination rate of photo-generated electron/hole pairs and inhibits the photocatalytic efficiency [60]. The highest photocatalytic efficiency was observed using citric acid ratio 4. The photocatalytic efficiencies of LFC4-300, LFC4-400, LFC4-500, LFC4-600 and LFC4-700 are 20.3, 30.8, 45.5, 41.5%, and 46.2% after two hours of reaction time, respectively. Meanwhile, after thirty minutes of reaction time, these catalytic efficiencies were dramatically increased to 52.9, 74.8, 99.6, 99.3, and 99.3% in the presence of 0.5 mM H_2O_2. We can conclude that the controlling of particle size of $LaFeO_3$ and residual carbon amount (as presented in FTIR (Fig. 2)

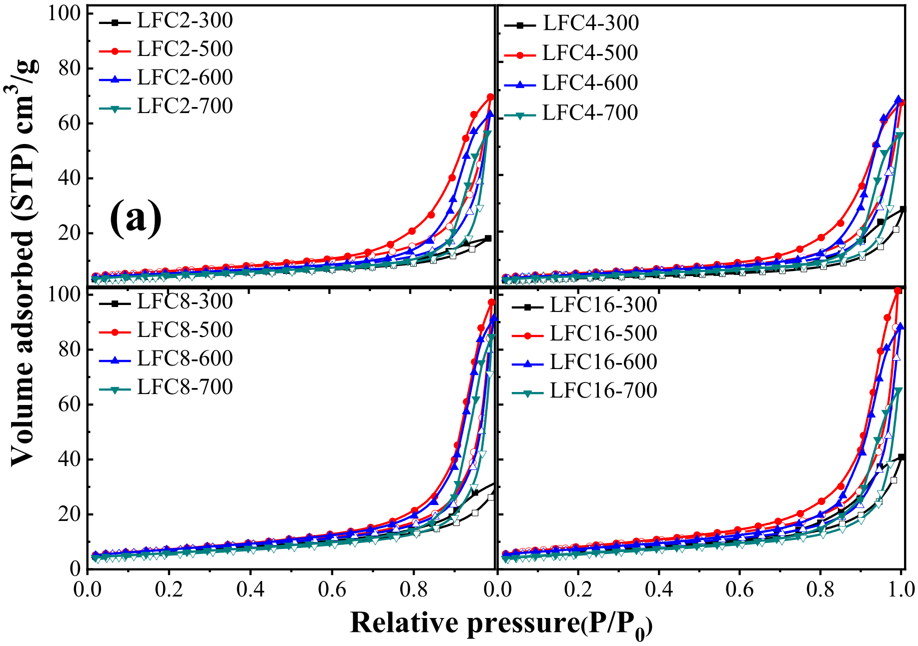

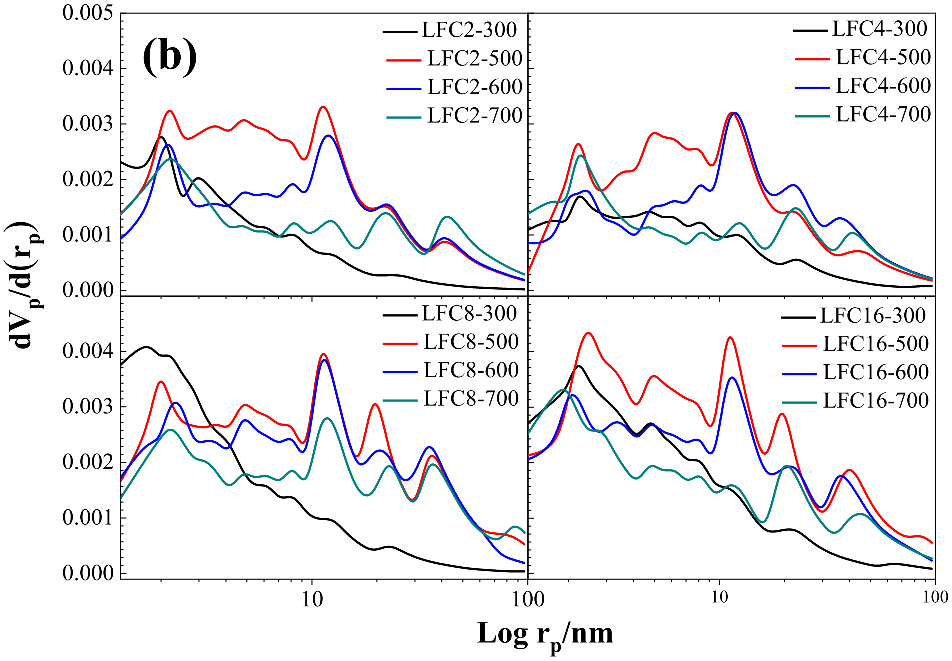

Fig. 6. (a) N_2 adsorption/desorption isotherm curves of $LaFeO_3$ samples synthesized using different molar ratios of citric acid and calcined at different temperatures. (b) Pore size distribution curves obtained with the adsorption branches of the above isotherms.

and TGA (Fig. 3)) are significant factors in the photocatalytic decolorization of organic contaminants because they could adjust the separation of photo-generated hole-electron pairs. In a high citric acid ratio, the particle size was decreased in all calcination temperatures. As a result, the recombination rate of photo-generated hole-electron pairs was increased and the photocatalytic process was suppressed even in presence of H_2O_2. This unexpected behavior of H_2O_2 is related to the acidic surface functional group in the carbon in the $LaFeO_3$ materials that retard H_2O_2 activity to produce $^{\bullet}OH$ and thus might decompose to H_2O and O_2 [61]. Wang *et al.* found the reduction of particle size for $NaNbO_3$ to a certain threshold (<30 nm) increases the recombination rate of photogenerated electron/hole pairs and decreases the photocatalytic efficiency [62]. The reduction of particle size might alter the geometry configuration of the surface and decrease the coordination number of the surface atoms which also leads to an increase in the number of defect sites and immobilization of more excitons on the sample surface.

To investigate the photocatalytic reaction mechanism of MB decolorization over $LaFeO_3$ NPs, 3% ethanol was added to the reaction mixture as shown in Fig. S5d. The photocatalytic efficiency of LFC4-500 was significantly suppressed to 1.35% and 10% after one hour in the absence and presence of 0.5 mM H_2O_2 under solar-light irradiation. Ethanol is known as a hole and hydroxyl radical ($^{\bullet}OH$) scavenger [44]. To investigate the dominant reactive species ca. electron, hole, and hydroxide radicals that responsible for MB decolorization over $LaFeO_3$ surface, different scavenger reagents such as sodium persulphate (PS), EDTA, and *t*-butyl alcohol (TB)

Table 4

Comparison of $LaFeO_3$ efficiency for decolorization of methylene blue *via* photocatalytic processes.

Catalyst	Reaction conditions	Degradation rate (%)	Time (min)	Reusability	Ref.
$LaFeO_3$	[MB] = 25 mg/L, $[H_2O_2]$ = 4.0 mM, Catalyst loading = 0.5 g/L, 400 W Hg lamp	33%	180	–	[46]
$CdS/LaFeO_3$		97.5%		93% after 5th cycles	
$LaFeO_3$	[MB] = 15 mg/L, $[H_2O_2]$ = 17.6 mM, pH 2, Catalyst loading = 0.02 g/L, Visible light irradiation	99.38%	60		[47]
$LaFeO_3$	[MB] = 10 mg/L, $[H_2O_2]$ = 176 mM, 500 W Xenon lamp with 420 nm cutoff filter as a visible light source.	93.8%	240	–	[48]
$LaFeO_3$	[MB] = 20 mg/L, Catalyst loading = 1.0 g/L, 300 W Xenon arc lamp	45.5%	180	39.3% after 3rd cycles	[49]
$LaFeO_3$/silica fiber		47.5%		–	
$LaFeO_3$	[MB] = 20 mg/L, Catalyst loading = 2 g /L, 400-W xenon lamp with a cut-off light below 400 and the light intensity per unit area was 450 mW/cm^2.	12.6%	60		[50]
$AgCl/Ag/LaFeO_3$		97.9%	100	No change after the 5th cycle	
$LaFeO_3$	[MB] = 5 mg/L, Catalyst loading = 2 g/L, high-pressure fluorescent Hg lamp (125 W)	59.79%	120	–	[51]
$LaFeO_3$	[MB] = 5 mg/L, Catalyst loading = 0.5 g/L, A 125 W high-pressure lamp (λmax = 365 nm) was used as light source	40%	150	–	[52]
$LaFeO_3$	[MB] = 0.5 mg/L, Catalyst loading = 0.1 g/L, 300 W xenon arc lamp with a UV-cutoff filter(400 nm)	No obvious efficiency	70	–	[53]
$LaFeO_3$-C		60%			
$LaFeO_3$-rGO		98%			
$LaFeO_3$	[MB] = 25 mg/L, Catalyst loading = 0.4 g/L , 400 W mercury lamp with a 420 nm cutoff filter	42%	240	–	[54]
$LaFeO_3$	[MB] = 10 mg/L, Catalyst loading = 0.5 g/L,40 W fluorescent Light(8.35 W·m − 2 at 420 nm)	48.9%	90	–	[55]
$LaFeO_3$/Ti foil	[MB] = 10 mg/L, A 500 W tungsten halogen lamp with the intensity of 130 mW cm^{-2}.	32.9%	120		[19]
$LaFeO_3/TiO_2$ NATs		69.7%			
$LaFeO_3$	[MB] = 5 mg/L, Catalyst loading = 1 g/L, 3 W LED irradiation	3%	120	–	[56]
5%-$LaFeO_3$/g-C_3N_4		>95%		No significant changes in catalytic efficiency after 4th cycles	
Bulk $LaFeO_3$	[MB]= ? Catalyst loading = 1 g/L, 150 W high pressure, mercury lamp(λ>400 nm)	7.4%	120		[57]
Floral like $LaFeO_3$		92.85%		No catalytic activity loss after 4th cycles	
$LaFeO_3$ NPs	[MB] = 10 mg/L, Catalyst loading = 0.2 g/L, pH = 3,1 75 W Xenon lamp (100 mW/cm^2) as a visible light source	45.6%	120	95.3% degradation efficiency after 5th cycles	In this work
	[MB] = 10 mg/L, $[H_2O_2]$ = 0.5 mM, Catalyst loading = 0.2 g/L, pH = 3, 75 W Xenon lamp (100 mW/cm^2)	99.6%	30		

were utilized, respectively (Fig. S8). In the presence of 2.0 mmoles of sodium persulphate, the photocatalytic efficiency of LFC4-500 and LFC16-500 was increased up to 100 and 50% within 30 min, indicating that the persulphate anion scavenge the photogenerated electrons and form $^{\bullet}SO_4^-$ species. By addition 2.0 mmoles of EDTA (as a hole scavenger), the photocatalytic efficiency of LFC-16-500 and LFC4-500 for MB decolorization was significantly enhanced up to 50% and 63% after two hours due to generation of more electrons reducing oxygen to superoxide radicals or formation hydrogen peroxide. These results indicated that the recombination rate of the photo-generated charge carriers for LFC-16-500 is higher than that of LFC4-500. Further, the photocatalytic efficiency was significantly suppressed over the LFC4-500 from 46% to 6% by addition of 2.0 mmoles TB. Based on these results, the photocatalytic decolorization of MB was dominated by the formation of $^{\bullet}OH$ radicals.

Next attention was turned to examine the charge transfer resistance (R_{ct}) and separation efficiency between the photo-generated electrons and holes by electrochemical impedance spectroscopy (EIS) in the range of 0.01 Hz to 100 kHz at E_{DC} = 0.5 V *vs.* Ag/AgCl and E_{AC} = 10 mV. Fig. S9 shows the Nyquist plot of LFC4-500 and LFC16-500 modified glassy carbon electrode (GCE) in the absence and presence of 10.0 mmole ascorbic acid in dark and light. A typical semicircle was observed for $LaFeO_3$ materials regarding charge transfer resistance. The LFC16-500 illustrates a smaller arc radius than LFC4-500, indicating a low charge transfer resistance of LFC16-500 in dark. As a result of the smaller particle size, the LFC16-500/GCE could easily oxidize ascorbic acid. In the absence of ascorbic acid, both $LaFeO_3$ materials demonstrated a decrease in charge transfer resistance (R_{ct}) after solar light irradiation owing to charge carrier immobilization. The arc radius of LFC4-500 was significantly reduced compared to LFC16-500 in in the presence of ascorbic acid. These findings might support LFC4-500 sensitivity to solar light irradiation, as well as its low charge transfer resistance and adequate separation of photo-generated electron and hole pairs for trapping in residual carbon.

The position of CB and VB band edges of semiconductors is an important factor for photocatalytic processes. The potential of CB and VB were calculated according to the *Mulliken* electronegativity theory, as E_{CB} = -0.19 eV, E_{VB} = 2.28 eV for LFC4-500. After solar irradiation, the $LaFeO_3$ NPs absorb visible light to generate electron and hole pairs. The suggested mechanism is demonstrated in Fig. S10. The electrons are transferred from VB to CB and leaving positive holes in VB as shown in Eq. (8). The photogenerated hole has more positive potential than $^{\bullet}OH/OH^-$ (1.99 eV *vs.* NHE) suggesting that the accumulated holes (2.28 eV *vs.* NHE) on the VB of $LaFeO_3$ can oxidize OH^- to $^{\bullet}OH$ which subsequently decolorizes MB dye (Equations (9) and (10)). The LUMO and HOMO levels of

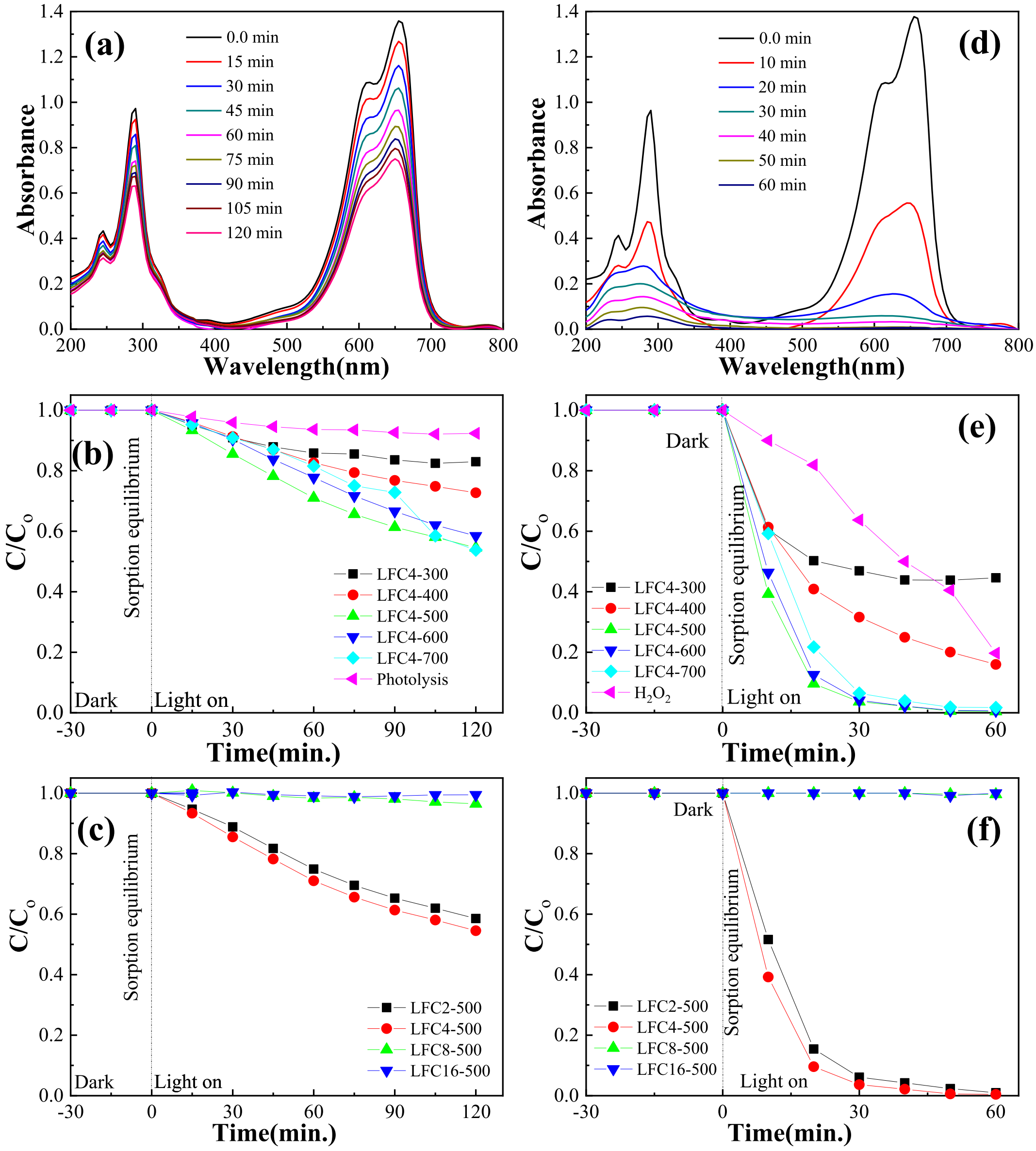

Fig. 7. Absorbance spectra of photocatalytic MB decolorization by LFC4-500 in (a) absence and (d) presence of 0.5 mM H_2O_2, (b, and e) Change of relative concentration for MB decolorization of LFC4-y at different calcination temperatures in (b) absence and (e) presence of 0.5 mM H_2O_2, and Change of relative concentration for MB decolorization of LFCx-500 at different citric acid ratios in (c) absence and (f) presence of 0.5 mM H_2O_2,

MB are −0.25 and 1.61 eV, respectively. Thus, the electron of LUMO could diffuse to CB of $LaFeO_3$. The photogenerated electrons in the conduction band (-0.19 eV *vs.* NHE) of $LaFeO_3$ are less negative than $O_2/^{\bullet}O_2^-$ (-0.33 eV *vs.* NHE) and cannot be able to reduce the O_2 to $^{\bullet}O_2^-$ which also proved that $^{\bullet}O_2^-$ radicals are not the reactive species. However, it could reduce the O_2 to H_2O_2 at (0.68 eV *vs.* NHE) which subsequently reduced the H_2O_2 to $^{\bullet}OH$ at 0.32 eV *vs.* NHE. Thus, the adsorbed oxygen on $LaFeO_3$ can be reduced by two-electrons to form H_2O_2 which is eventually reduced by one-electron to form $^{\bullet}OH$ and OH^- (Eqs. (11) and (12)). The addition of a suitable amount of H_2O_2, facilitate the generation of $^{\bullet}OH$ and promote decolorization efficiency (Eq. (13)). At the same time, the hydrogen peroxide could react with the $LaFeO_3$ catalyst and may cause a reduction of Fe^{3+} to Fe^{2+} which participate in the Fenton-like reaction (Eqs. (14)–(17)) [24].

$$LaFeO_3 + h\nu \rightarrow e^- + h^+ \tag{8}$$

$$H_2O + h^+ \rightarrow {}^{\bullet}OH + H^+ \tag{9}$$

$$OH^- + h^+ \rightarrow {}^{\bullet}OH \tag{10}$$

$$O_2 + 2H^+ + 2e^- \rightarrow H_2O_2 \tag{11}$$

$$H_2O_2 + e^- \rightarrow {}^{\bullet}OH + OH^- \tag{12}$$

$$H_2O_2 + h\nu \rightarrow 2\,{}^{\bullet}OH \tag{13}$$

$$=Fe^{3+} + H_2O_2 \rightarrow = Fe^{3+} - H_2O_2 \tag{14}$$

$$= Fe^{3+} - H_2O_2 \rightarrow =Fe^{2+} + HO_2^{\bullet} + H^+ \tag{15}$$

$$=Fe^{3+} + HO_2^{\bullet} \rightarrow =Fe^{2+} + O_2 + H^+ \tag{16}$$

$$=Fe^{2+} + H_2O_2 \rightarrow =Fe^{3+} + {}^{\bullet}OH + OH^- \tag{17}$$

$$\text{Dye} + {}^{\bullet}OH \rightarrow \text{decolorization products} \tag{18}$$

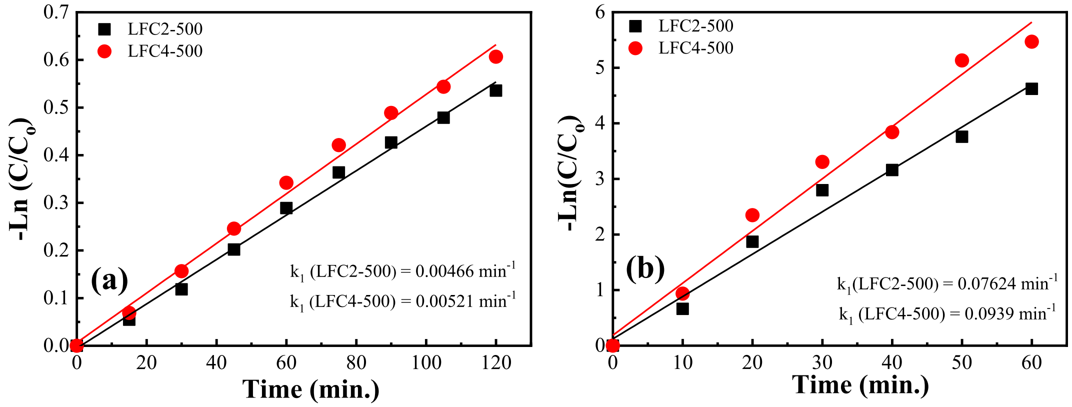

Fig. 8. The integrated first-order reaction rate of the photocatalytic MB decolorization at 500 °C and citric acid ratios 2, and 4 in (a) absence and (b) presence of 0.5 mM H_2O_2.

Based on the above results, the $^{\bullet}OH$ has a key role in photocatalytic decolorization of MB (Eq. (18)). The photocatalytic rates were explored *by* applying first and second-order reaction equations (Fig. 8). It was found the photocatalytic reaction rate was fitted by the pseudo-first-order reaction. The rat of photocatalytic reaction value was estimated and found to be 0.0047, 0.0052, 0.076, and 0.094 min^{-1} for LFC2-500, LFC4-500, LFC2-500/H_2O_2 and, LFC4-500/H_2O_2, respectively. The rate of reaction was LFC4-500 is higher than LFC2-500. Besides, the photocatalytic rate for LFC4-500 was enhanced more than eighteen times in the presence of 0.5 mM H_2O_2. These results were also confirmed through the measurement of Fe^{3+} concentration that leached through the photocatalytic process. After the photo-Fenton-like catalytic experiment, the filtrate was collected and analyzed using ICP-MS. The concentrations of leached Fe^{3+} metals were found to be 2.0 mg/L for LFC4-500. The leached Fe^{3+} metal is about 1% of the total $LaFeO_3$ dosage. This negligible concentration of dissolved ferric ions implied that no significant contribution of homogenous photo-Fenton-like reaction might occur.

The stability and reusability of the $LaFeO_3$ catalyst is a major advantage in the development of applicable catalyst. The recycling of the LFC4-500 catalyst was evaluated by performing the photocatalytic decolorization of MB experiment several times. In each experiment, the LFC4-500 catalyst separated by the centrifuge, washed with ethanol/water mixture, and then dried in an oven at 60 °C overnight. The LFC4-500 catalyst showed excellent reusability with no significant change in the efficiency even after five cycles as shown in Fig. 9. The estimated efficiency calculated to be more than 98%, indicating that, the $LaFeO_3$ catalyst maintains its features after five cycles. The results demonstrate also that it is possible to produce a reusable, economical, and efficient $LaFeO_3$ catalyst by adjusting the citric acid ratio for intensive photocatalytic processes.

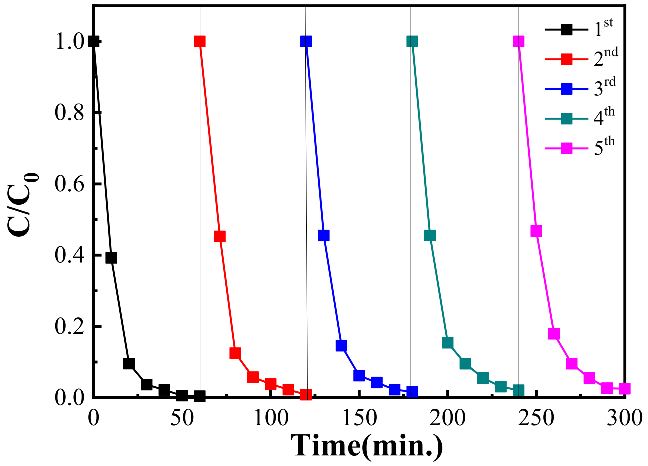

Fig. 9. Reusability of LFC4-500 in the photocatalytic degradation of methylene blue in presence of 0.5 mM H_2O_2. (For interpretation of the references to color in this figure legend, the reader is referred to the web version of this article.)

4. Conclusions

We have successfully synthesized size-controlled $LaFeO_3$ NPs by using different citric acid: metal ions ratio *via* a direct sol-gel auto-combustion method. It was found that the employed citric acid ratios (2, 4, 8, and 16) and calcination temperatures (300, 500, 600, and 700 °C) were playing a significant role in the formation of targeted $LaFeO_3$ NPs. Thus, the formation of different L (citrate): M (Fe and/or La) at low and high M: L ratios affect the size, structure and properties of the produced NPs. The formed $LaFeO_3$ NPs obtained with different citric acid ratios showed different behavior toward the decolorization of MB in the absence and presence of H_2O_2 under-stimulated solar light irradiation. Among the formed $LaFeO_3$, the sample LFC4-500 showed promising photocatalytic efficiency, stability, and reusability for photocatalytic processes. Furthermore, the formation of highly reactive hydroxide radicals ($^{\bullet}OH$) *via* heterogeneous photo-Fenton-like reaction dominates the photocatalytic pathway. Thus, the complex-assisted sol-gel method could be employed as an efficient method and economical protocol to synthesize highly photoactive perovskite materials. The results also indicated the importance of $LaFeO_3$ as a promising photo-Fenton-like catalyst and their prospective application as heterogeneous catalysts for the decolorization of various organics in wastewater.

Declaration of Competing Interest

The authors declare that they have no known competing financial interests or personal relationships that could have appeared to influence the work reported in this paper.

Appendix A. Supplementary data

Supplementary data to this article can be found online at https://doi.org/10.1016/j.apt.2022.103429.

References

[1] J. Ma, H. Hung, C. Tian, R. Kallenborn, Revolatilization of persistent organic pollutants in the Arctic induced by climate change, Nat. Clim. Change 1 (2011) 255–260.

[2] M. Khairy, S.A. El-Safty, M. Ismael, H. Kawarada, Mesoporous NiO nanomagnets as catalysts and separators of chemical agents, Appl. Catal., B 127 (2012) 1–10.

[3] K.M.S. Khalil, O.A.S. Allam, M. Khairy, K.M.H. Mohammed, R.M. Elkhatib, M.A. Hamed, High surface area nanostructured activated carbons derived from sustainable sorghum stalk, J. Mol. Liq. 247 (2017) 386–396.

[4] Y. Ahmed, Z. Yaakob, P. Akhtar, Degradation and mineralization of methylene blue using a heterogeneous photo-Fenton catalyst under visible and solar light irradiation, Catal. Sci. Technol. 6 (2016) 1222–1232.

[5] D. Kanaujiya, T. Paul, A. Sinharoy, K. Pakshirajan, Biological Treatment Processes for the Removal of Organic Micropollutants from Wastewater: a Review, Curr. Pollution Rep. 5 (2019) 112–128.

[6] Y. Yang, G. Banerjee, G. Brudvig, J.-H. Kim, J. Pignatello, Oxidation of Organic Compounds in Water by Unactivated Peroxymonosulfate, Environ. Sci. Technol. 52 (2018) 5911–5919.

[7] Z. Cao, M. Qin, B. Jia, Y. Gu, P. Chen, A. Volinsky, X. Qu, One-pot solution combustion synthesis of highly mesoporous hematite for photocatalysis, Ceram. Int. 41 (2015) 2806–2812.

[8] L.M. Pastrana-Martínez, N. Pereira, R. Lima, J.L. Faria, H.T. Gomes, A.M.T. Silva, Degradation of diphenhydramine by photo-Fenton using magnetically recoverable iron oxide nanoparticles as catalyst, Chem. Eng. J. 261 (2015) 45–52.

[9] Y. Wu, R. Chen, H. Liu, Y. Wei, D. Wu, Feasibility and mechanism of *p*-nitrophenol decomposition in aqueous dispersions of ferrihydrite and H_2O_2 under irradiation, Reac. Kinet. Mech. Cat. 110 (2013) 87–99.

[10] S. Jauhar, S. Singhal, M. Dhiman, Manganese substituted cobalt ferrites as efficient catalysts for H_2O_2 assisted degradation of cationic and anionic dyes: Their synthesis and characterization, Appl. Catal. A 486 (2014) 210–218.

[11] Q. Liu, Y. Zhou, L. You, J. Wang, M. Shen, L. Fang, Enhanced ferroelectric photoelectrochemical properties of polycrystalline $BiFeO_3$ film by decorating with Ag nanoparticles, Appl. Phys. Lett. 108 (2016) 022902.

[12] Z. Li, Y. Shen, Y. Guan, Y. Hu, Y. Lin, C.-W. Nana, Band gap engineering and enhanced interface coupling of graphene–$BiFeO_3$ nanocomposites as efficient photocatalysts under visible light, J. Mater. Chem. A 2 (2014) 1967–1973.

[13] J. Yang, R. Li, X. Li, Y. Long, J. Zhou, Y. Zhang, Molten salt synthesis of $SrFeO_3$ nanocrystals, J. Ceram. Soc. Jpn. 119 (2011) 736–739.

[14] H. Lim, J. Lee, S. Jin, J. Kim, J. Yoon, T. Hyeon, Highly active heterogeneous Fenton catalyst using iron oxide nanoparticles immobilized in alumina coated mesoporous silica, Chem. Commun. 4 (2006) 463–465.

[15] P. Nidheesh, Heterogeneous Fenton catalysts for the abatement of organic pollutants from aqueous solution: a review, RSC Adv. 5 (2015) 40552–40577.

[16] J. Herney-Ramirez, M.A. Vicente, L.M. Madeira, Heterogeneous photo-Fenton oxidation with pillared clay-based catalysts for wastewater treatment, Appl. Catal., B 98 (2010) 10–26.

[17] Z.-T. Hu, S.K. Lua, T.-T. Lim, Cuboid-like $Bi_2Fe_4O_9$/Ag with Graphene-Wrapping Tribrid Composite with Superior Capability for Environmental Decontamination: Nanoscaled Material Design and Visible-Light-Driven Multifunctional Catalyst, ACS Sustainable Chem. Eng. 3 (2015) 2726–2736.

[18] E. Grabowska, Selected perovskite oxides: Characterization, preparation and photocatalytic properties, Appl. Catal., B 186 (2016) 97–126.

[19] C. Gong, Z. Zhang, S. Lin, Z. Wu, L. Sun, C. Ye, Y. Hu, C. Lin, Electrochemical synthesis of perovskite $LaFeO_3$ nanoparticle-modified Ti_O2 nanotube arrays for enhanced visible-light photocatalytic activity, New J. Chem. 43 (2019) 16506–16514.

[20] M. Scafetta, A. Cordi, J.M. Rondinelli, S.J. May, Band structure and optical transitions in $LaFeO_3$: theory and experiment, J. Phys.: Condens. Matter 26 (2014) 505502–505509.

[21] T. Vijayaraghavan, R. Sivasubramanian, S. Hussain, A. Ashok, A Facile Synthesis of $LaFeO_3$ -Based Perovskites and Their Application towards Sensing of Neurotransmitters, ChemistrySelect 2 (2017) 5570–5577.

[22] P. Wang, Y. He, Y. Mi, J. Zhu, F. Zhang, Y. Liu, Y. Yang, M. Chen, D. Cao, Enhanced photoelectrochemical performance of $LaFeO_3$ photocathode with Au buffer layer, RSC Adv. 9 (2019) 26780–26786.

[23] S. Thirumalairajan, K. Girija, I. Ganesh, D. Mangalaraj, C. Viswanathan, A. Balamurugan, N. Ponpandian, Controlled synthesis of perovskite $LaFeO_3$ microsphere composed of nanoparticles via self-assembly process and their associated photocatalytic activity, Chem. Eng. J. 209 (2012) 420–428.

[24] T. Phan, A. Nikoloski, P. Bahri, Dan Li, Adsorption and photo-Fenton catalytic degradation of organic dyes over crystalline $LaFeO_3$-doped porous silica, RSC Adv. 8 (2018) 36181–36190.

[25] F. Taylor, J. Buckeridge, C. Catlow, Defects and Oxide Ion Migration in the Solid Oxide Fuel Cell Cathode Material $LaFeO_3$, Chem. Mater. 28 (22) (2016) 8210–8220.

[26] X. Qi, J. Zhou, Z. Yue, Z. Gui, L. Li, A simple way to prepare nanosized $LaFeO_3$ powders at room temperature, Ceramics Int. 29 (2003) 347–349.

[27] S. Farhadi, N. Rashidi, Microwave-induced solid-state decomposition of the Bi $[Fe(CN)_6]\cdot 5H_2O$ precursor: A novel route for the rapid and facile synthesis of pure and single-phase $BiFeO_3$ nanopowder, J. Alloys Compd. 503 (2010) 439–444.

[28] N. Sharmaa, S. Sharma, K. Sachdev, Effect of precursors on the morphology and surface area of $LaFeO_3$, Ceram. Int. 45 (2019) 7217–7225.

[29] M. Sivakumar, A. Gedanken, W. Zhong, Y. Jiang, Y. Du, B. Brukental, D. Bhattacharya, Y. Yeshurunc, I. Nowikd, Sonochemical synthesis of nanocrystalline $LaFeO_3$, J. Mater. Chem. 14 (2004) 764–769.

[30] M. Kumar, S. Srikanth, B. Ravikumar, T. Alex, S. Das, Synthesis of pure and Sr-doped $LaGaO_3$, $LaFeO_3$ and $LaCoO_3$ and Sr, Mg-doped $LaGaO_3$ for ITSOFC application using different wet chemical routes, Mater. Chem. Phys. 113 (2009) 803–815.

[31] K. Khalil, W. Elhamdy, A. Saied, A. Elsamahy, Porous LaFeO3/Silica Nanocomposites via Sol-Gel Mixing Involving Citric Acid, Colloids Surf., A 506 (2016) 840–848.

[32] K.M.S. Khalil, W.A. Elhamdy, A.A. Said, Direct formation of LaFeO3/MCM−41 nanocomposite catalysts and their catalytic reactivity for conversion of isopropanol, Mater. Chem. Phys. 254 (2020) 123412.

[33] K. Wang, H. Niu, J. Chen, J. Song, C. Mao, S. Zhang, Y. Gao, Immobilizing $LaFeO_3$ nanoparticles on carbon spheres for enhanced heterogeneous photo-Fenton like performance, Appl. Surf. Sci. 404 (2017) 138–145.

[34] R. Köferstein, L. Jäger, S. Ebbinghaus, Magnetic and optical investigations on $LaFeO_3$ powders with different particle sizes and corresponding ceramics, Solid State Ionics 249–250 (2013) 1–5.

[35] P. Gosavi, R. Biniwale, Pure phase LaFeO3 perovskite with improved surface area synthesized using different routes and its characterization, Mater. Chem. Phy. 119 (2010) 324–329.

[36] J. Feng, T. Liu, Y. Xu, J. Zhao, Y. He, Effects of PVA content on the synthesis of LaFeO3 via sol-gel route, Ceram. Int. 37 (2011) 1203–1207.

[37] Q. Lin, X. Yang, J. Lin, Y. He, J. Dong, L. Wang, The Influence of Ba2+ Ions on the Physical Properties of Perovskite Nanoparticles La1-xBaxFeO3 Synthesized by Sol-Gel Method, Phys. Status Solidi B 257 (2020) 1900597.

[38] A. Silva, X. Kong, M. Parkin, R. Cammack, R. Hider, Iron(III) citrate speciation in aqeous solution, Dalton Trans. 40 (40) (2009) 8616–8625.

[39] G. Luneau, C. Merle, D. Phanon, C. Lebrun, F. Biaso, G. Serratrice, G. Serratrice, J.-L. Pierre, New Trends in the Chemistry of Iron(iii) Citrate Complexes: Correlations between X-ray Structures and Solution Species Probed by Electrospray Mass Spectrometry and Kinetics of Iron Uptake from Citrate by Iron Chelators, Chem. Eur. J. 11 (2005) 2207–2219.

[40] T. McLean, in: A.F. Gibson (Ed.), Progress in Semiconductors 5 (1960) 55–102.

[41] K. Parida, K. Reddy, S. Martha, D. Das, N. Biswal, Fabrication of nanocrystalline $LaFeO_3$: An efficient sol-gel auto-combustion assisted visible light responsive photocatalyst for water decomposition, Int. J. Hydrogen Energy 35 (2010) 12161–12168.

[42] Q. Qin, Y. Liu, X. Li, T. Suna, Y. Xu, Enhanced heterogeneous Fenton-like degradation of methylene blue by reduced $CuFe_2O_4$, RSC Adv. 8 (2018) 1071–1077.

[43] K. Dutta, S. Mukhopadhyay, S. Bhattacharjee, B. Chaudhuri, Chemical oxidation of methylene blue using a Fenton-like reaction, J. Hazard. Mater. 84 (2001) 57–71.

[44] J. Schneider, D.W. Bahnemann, Undesired Role of Sacrificial Reagents in Photocatalysis, J. Phys. Chem. Lett. 4 (2013) 3479–3483.

[45] X. Xin, J. Lang, T. Wang, Y. Su, Y. Zhao, X. Wang, Construction of novel ternary component photocatalyst $Sr_{0.25}H_{1.5}Ta_2O_6\cdot H_2O$ coupled with g-C_3N_4 and Ag toward efficient visible light photocatalytic activity for environmental remediation, Appl. Catal., B 181 (2016) 197–209.

[46] A. Hoseini, S. Farhadi, A. Zabardasti, F. Siadatnasab, A novel n-type CdS nanorods/p-type LaFeO3 heterojunction nanocomposite with enhanced visible-light photocatalytic performance, RSC Adv. 9 (2019) 24489–24504.

[47] S. Jauhar, M. Dhiman, S. Bansal, S. Singhal, Mn^{3+} ion in perovskite lattice: a potential Fenton's reagent exhibiting remarkably enhanced degradation of cationic and anionic dyes, J. Sol-Gel Sci. Technol. 75 (2015) 124–133.

[48] H. Shen, T. Xue, Y. Wang, G. Cao, Y. Lu, G. Fang, Photocatalytic property of perovskite LaFeO3 synthesized by sol-gel process and vacuum microwave calcination, Mater. Res. Bull. 84 (2016) 15–24.

[49] L. Zhang, T. Xu, Q. Guo, Z. Ling, R. Zou, Q. Wu, Enhanced photocatalytic efficiencies over A- or B-sites substituted $LaFeO_3$/silica fiber composites, J. Phys. Chem. Solids 110 (2017) 136–144.

[50] X. Gao, Y. Shang, L. Liu, W. Nie, F. Fu, AgCl/Ag/$LaFeO_3$ heterojunction with a prolonged charge lifetime and enhanced visible-light catalytic property, J. Phys. Chem. Solids 127 (2019) 186–193.

[51] S. Li, M. Guo, X. Wang, K. Gao, Fabrication and photocatalytic activity of $LaFeO_3$ ribbon-like nanofibers, J. Chin. Chem. Soc. 67 (2020) 990–997.

[52] S. Dong, K. Xu, G. Tian, Photocatalytic activities of $LaFe_{1-x}Zn_xO_3$ nanocrystals prepared by sol-gel auto-combustion method, J. Mater. Sci. 44 (2009) 2548–2552.

[53] X. Ren, H. Yang, S. Gen, J. Zhou, T. Yang, X. Zhang, Z. Chenga, S. Sun, Controlled growth of $LaFeO_3$ nanoparticles on reduced graphene oxide for highly efficient photocatalysis, Nanoscale 8 (2016) 752–756.

[54] S. Farhadi, M. Amini, F. Mahmoudia, Phospho tungstic acid supported on amino silica functionalized perovskite-type $LaFeO_3$ nanoparticles: a novel recyclable and excellent visible-light photocatalyst, RSC Adv. 6 (2016) 102984–102996.

[55] F. Li, Y. Liu, R. Liu, Z.-M. Sun, D.-S. Zhao, C. Kou, Preparation of Ca-doped $LaFeO_3$ nanopowders in a reverse microemulsion and their visible-light photocatalytic activity, Mater. Lett. 64 (2010) 223–225.

[56] K. Xua, J. Feng, Superior photocatalytic performance of $LaFeO_3$/g-C_3N_4 heterojunction nanocomposites under visible light irradiation, RSC Adv. 7 (2017) 45369–45376.

[57] S. Thirumalairajan, K. Girija, V. Mastelaro, N. Ponpandian, Photocatalytic degradation of organic dyes under visible light irradiation by floral-like $LaFeO_3$ nanostructures comprised of nanosheet petals, New J. Chem. 38 (2014) 5480–5490.

[58] S.A. Khan, Z. Arshad, S. Shahid, I. Arshad, K. Rizwan, M. Sher, U. Fatima, Synthesis of TiO2/Graphene oxide nanocomposites for their enhanced

photocatalytic activity against methylene blue dye and ciprofloxacin, Compos. Part B: Eng. 175 (2019) 107120.

[59] X. Yu, L. Huang, Y. Wei, J. Zhang, Z. Zhao, W. Dai, B. Yao, Controllable preparation, characterization and performance of Cu_2O thin film and photocatalytic degradation of methylene blue using response surface methodology, Mater. Res. Bull. 64 (2015) 410–417.

[60] L. Zhang, H.H. Mohamed, R. Dillert, D. Bahnemann, Kinetics and mechanisms of charge transfer processes in photocatalytic systems, J. Photoch. Photobiol. C 13 (2012) 263–276.

[61] G. Fang, C. Liu, J. Gao, D. Zhou, New Insights into the Mechanism of the Catalytic Decomposition of Hydrogen Peroxide by Activated Carbon: Implications for Degradation of Diethyl Phthalate, Ind. Eng. Chem. Res. 53 (2014) 19925–19933.

[62] X. Li, Q. Li, L. Wang, The effects of $NaNbO_3$ particle size on the photocatalytic activity for 2-propanol photodegradation, Phys. Chem. Chem. Phys. 15 (2013) 14282–14289.